One-Step Sol-Gel Facile Synthesis and 3D Nanoscale Morphology Investigation of $Bi_{0.5}Na_{0.5}TiO_3$-$BaTiO_3$ Thin Films

Carlos Yago Pereira Batista[1,2], Yurimiler Leyet Ruiz[2] and Henrique Duarte da Fonseca Filho[3,*]

[1]*Instituto de Inovação, Pesquisa Desenvolvimento Cientifico e Tecnologico do Amazonas, IPDEC, Centro, Manaus - AM, 69010-000*

[2]*Technological Materials Processing Laboratory, Federal University of Amazonas, Manaus, Amazonas, 69067-005, Brazil*

[3]*Laboratory of Nanomaterials Synthesis and Nanoscopy, Department of Physics, Federal University of Amazonas, Manaus, Amazonas, 69067-005, Brazil*

Abstract: Bismuth sodium titanate, denoted as $Bi_{0.5}Na_{0.5}TiO_3$-$BaTiO_3$ (BNT-BT), possessing a perovskite-like structure, has emerged as a highly prospective material in recent years. It is considered a prime contender for replacing PZT-based compounds due to its exceptional piezoelectric and ferroelectric properties, coupled with the presence of loosely bound pairs of chemically active electrons. This study delves into the micromorphological properties of BNT-BT thin film electrodes, fabricated using sol-gel spin-coating and subsequent annealing processes. Employing Atomic Force Microscopy (AFM), comprehensive 2D and 3D topographical maps were acquired, enabling the extraction of pivotal parameters crucial for surface characterization. Notably, the investigation encompasses Minkowski Functionals, which encompass normalized Minkowski volume, boundary, and connectivity analyses. In conjunction, various roughness parameters, encompassing arithmetic mean height, maximum peak height, maximum valley depth, arithmetic mean depth, and the ten-point height parameter, were quantified across these analyses to facilitate a comprehensive comparison of surface morphologies among distinct samples. The morphological analysis outcome underscores the potential for elucidating material performance through microstructural shape and quantitative roughness evaluation of respective surfaces. This holds significant promise for applications such as predictive assessment of functional behavior, including industrial quality control during sample manufacturing processes.

Keywords: BNT-BT, Thin films, Annealing, AFM, Roughness, Minkowski functionals.

1. INTRODUCTION

In recent decades, significant efforts in the scientific community have been directed towards comprehending and investigating the novel physical phenomena that emerge as a consequence of surface influences and interfacial interactions in such materials [1-3] A crucial aspect of surface engineering involves precisely manipulating grain size and boundaries in nanocrystalline thin films and ceramics, allowing the tailored adjustment of properties to meet diverse technological demands. Thin films have gained extensive utilization in electronic and microelectronic systems. Among the prevalent materials, lead-based compounds have dominated due to their exceptional piezoelectric attributes [4]. However, the considerable toxicity of lead in these materials has raised health and environmental concerns. Consequently, the pursuit of lead-free piezoelectric materials has become of utmost importance [5]. One notable contender in recent years for replacing lead-based compounds, particularly lead zirconate titanate (PZT), is bismuth sodium titanate (BNT). BNT exhibits promising piezoelectric and ferroelectric characteristics [6], along with the presence of free pairs of chemically active electrons [7]. With its perovskite-like structure, BNT has emerged as a favored candidate for PZT replacement owing to its robust ferroelectric properties [8].

Nevertheless, it's worth noting that while pure $Bi_{0.5}Na_{0.5}TiO_3$ (BNT) ceramics possess piezoelectric and ferroelectric properties, these values tend to be lower than those observed in PZT [7]. A strategy to address this discrepancy involves incorporating additional compounds into the BNT system to establish solid solutions, such as $BaTiO_3$ (BT) [7]. In recent years, an intriguing alternative has surfaced, yielding promising outcomes in material development. Compounds like $Bi_{0.5}Na_{0.5}TiO_3$-$BaTiO_3$ (BNT-BT) and $Bi_{0.5}Na_{0.5}TiO_3$-$Bi_{0.5}K_{0.5}TiO_3$ (BNT-BKT), have garnered attention as solid solutions, showcasing characteristics bordering on the morphotropic phase. These compositions not only suppress electrical conductivity but also enhance the piezoelectric traits of the materials, as evidenced by previous research [9].

Within the array of surface characterization methodologies, atomic force microscopy (AFM) stands as a potent technique for acquiring comprehensive

*Address correspondence to this author at the Laboratory of Nanomaterials Synthesis and Nanoscopy, Department of Physics, Federal University of Amazonas, Manaus, Amazonas, 69067-005, Brazil; Tel: 5592981019770;
E-mail: hdffilho@ufam.edu.br

E-ISSN: 2410-4701/23

three-dimensional (3D) topographic representations of surfaces [10, 11]. Furthermore, a multitude of approaches have come to fruition and solidified their presence in the past decade, facilitating the examination of 3D AFM maps for the discrimination and quantification of key parameters pivotal in evaluating the intricacies of surface roughness [12-17]. These methodologies encompass the determination of Minkowski functionals [12, 13], fractal [14, 15], and multifractal [16, 17] analyses, among other insightful techniques. Batista *et al*. recently presented the kinetics of ciprofloxacin reduction in $Bi_{0.5}Na_{0.5}Ba(TiO_3)_2$ electrocatalytic thin films, influenced by structural and micromorphological conditions [18]. XRD analysis revealed rhombohedral and tetragonal coexistence in 600, 650, and 700°C annealed BNT-BT films, with the former exhibiting more defects, confirmed by Raman spectroscopy. An increase in annealing temperature (600-700°C) didn't significantly alter topography, but 600°C annealed BNT-BT films displayed anisotropic microtexture with spatial complexity and low frequencies [18].

Hence, this manuscript embarks on an exploration of the 3D nanoscale surface characteristics of thin films composed of $Bi_{0.5}Na_{0.5}Ba(TiO_3)_2$, with the goal of revealing unique spatial arrangements. To accomplish this objective, we employed the sol-gel method to synthesize $Bi_{0.5}Na_{0.5}Ba(TiO_3)_2$ and subsequently deposited these films onto a Pt (111) (150 nm)/Ti (70 nm)/SiO_2 (500 nm)/Si (1 mm) substrate. In an innovative approach, we utilized Atomic Force Microscopy (AFM) to scrutinize the topographical spatial features and patterns of these films using the Minkowski Functionals (MFs), a method previously unexplored in this context. Concurrently, we assessed morphological parameters in accordance with the established guidelines outlined in ISO 25178-2:2012. It is noteworthy that our utilization of AFM and MFs represents a pioneering contribution as these methodologies have not been documented in prior research for this system.

2. MATERIALS AND METHODS

2.1. Synthesis of BNT-BT and Thin Films Deposition

To create the BNT-BT precursor solution, a systematic procedure was followed. Bismuth nitrate (Synth, P.A.), Barium Carbonate (Sigma-Aldrich, ≥99%), Sodium Hydroxide (Sigma-Aldrich ≥97%), and Titanium isopropoxide (Sigma-Aldrich, ≥97%) served as initial materials. Ethylene glycol, ethyl alcohol (J.T. Baker 99.8% PA), nitric acid (Neon, 65% P.A/ACS), and acetic acid (Sigma-Aldrich, ≥99%) acted as solvents. Citric acid (Synth ≥90%) was employed as ligands. For the BNT solution, a blend of $Ti[OCH(CH_3)_2]_4$, isopropyl alcohol, and ethylene glycol in a 1:3:3 (by weight) ratio was initially prepared. Glacial acetic acid was then introduced into this mixture. $Bi(NO_3)_3{\cdot}5H_2O$ was dissolved in the resultant solution, and a volume of isopropyl alcohol equivalent to the combined volume of citric acid, glacial acetic acid, and nitric acid in a 4:2:1 molar ratio mixture was added. Subsequently, NaOH was dissolved in the solution. To account for potential sodium loss through evaporation during high-temperature annealing, an excess of sodium (10 mol%) was incorporated. The BT solution was concocted using $Ba(CH_3COO)_2$ and $Ti[OCH(CH_3)_2]_4$ in a manner closely resembling the BNT solution procedure outlined above. Finally, $HN(CH_2CH_2OH)_2$ was introduced in appropriate quantities into both the BNT and BT solutions, followed by stirring for 2 hours. The BNT and BT solutions were then amalgamated and stirred for an additional 12 hours to yield the BNT-BT precursor solution.

The BNT-BT precursor solutions were applied onto Pt(111)/TiO_2/SiO_2/Si substrates using a spin-coating apparatus, which were prepared in triplicate from the solutions. Each layer was uniformly deposited at 3000 rpm for 60 seconds, followed by a brief drying phase at 80°C for one minute. A preliminary sintering step at 350°C for 10 minutes was carried out. This sequential process was repeated five times to achieve films with an approximate thickness of 200 nm. Subsequently, the films produced from each solution variant underwent separate annealing processes to allow the control of the desired structure [19]. Specifically, the S600 films were annealed at 600°C, the S650 films at 650°C, and the S700 films at 700°C. Each annealing step lasted for one hour. After completion, the films were gradually cooled down to room temperature (25°C) within an ambient air atmosphere.

2.2. 3D Nanoscale Surface Analysis by Atomic Force Microscopy (AFM)

Topographic mapping was executed using an atomic force microscope model Innova (Bruker) operating in tapping mode. A standard silicon cantilever RFESPA (Bruker) was employed, featuring parameters including a spring constant of approximately 3 N/m, a tip radius of about 8 nm, and a frequency around 75 kHz. The scanning process followed a linear rate of 0.5 Hz (equivalent to 1 line per second), utilizing a pixel

resolution of 256 × 256. The mapping encompassed a material area of 2.5 x 2.5 μm². To facilitate the imaging process, samples were sectioned into rectangular pieces measuring 2 x 2 cm² and affixed onto glass plates using double-sided tape. Subsequently, the acquired images underwent analysis through Gwyddion 2.59 software [20, 21]. This analysis was conducted in accordance with ISO standard 25178-2:2012, akin to prior recent studies (*e.g.*, [14, 22-25]). A wide array of height parameters was computed and investigated within this study. These parameters encompassed average roughness (Sa), maximum height of a peak (Sp), indicating the highest point on the surface; maximum depth of a valley (Sv), representing the lowest point within a depression; and the arithmetic mean value of the single roughness depths (Sz), which offers insight into the general surface roughness. These parameters were computed directly from the height distribution function $h(i, j)$ and are described according to Eqs. 1, and 2.

$$Sa = \frac{1}{N^2}\sqrt{\sum_{i,j=1}^{N}|h(i,j) - \langle h(i,j)\rangle|} \quad (1)$$

$$Sz = Sp + Sv \quad (2)$$

where N is the number of points used.

In addition to these parameters, the investigation delved into further morphological descriptors at the nanoscale. This involved the calculation of three Minkowski Functionals. The first functional is the volume (V) which is a measure of the relative amount of matter existing above the relative height. The second one pertained to boundaries distributions (S), which provides information about surface features and their distribution. The last functional, connectivity (χ), specifically the Euler-Poincaré characteristic, was also computed. This characteristic describes the connectivity of structures within the surface, offering a deeper understanding of its complex topology. All measurements were made from three different regions to obtain the errors in measured parameters.

3. RESULTS AND DISCUSSION

The surface characteristics of thin films are influenced by their structural properties, which can have a significant impact on their interactions with other materials. Given these circumstances, the utilization of AFM (Atomic Force Microscope) image processing for acquiring stereometric surface parameters has been the subject of extensive research in recent years [26-29]. These measurements offer valuable insights into various critical aspects of a surface, including but not limited to its roughness, distribution of peaks, hill and pit regions, and Minkowsky Functionals. Understanding these aspects, both qualitatively and quantitatively, is crucial for gaining insights into the morphology and microtexture of a surface. In this study, we extensively analyzed the spatial features of BNT-BT thin films to comprehend their behavior during potential interactions with other systems. The 2D and 3D surface topography of these films is depicted in Figure **1a**-**c** and Figure **1d**-**f**, respectively, revealing noticeable changes induced by heat treatment. Notably, S600 exhibits a smoother surface compared to S650 and S700. The transition from S600 to S650 illustrates a significant morphology shift, implying grain coalescence due to elevated temperatures. Interestingly, the morphology of S650 (Figure **3b**) resembles that of a Mn2+-doped BNT-BT system [30], while S700 resembles a $Bi_{0.5}Na_{0.5}TiO_3$–$BaTiO_3$–$SrTiO_3$ (BNT–BT–ST) system [31].

On a perfectly flat surface, the average roughness (Sa) is equal to zero, although surfaces with different Sa values can be easily designed, resulting in height variations due to the presence of peaks and valleys throughout the topography. This situation is what happens in the samples studied here, and already presented in Figure **1**. As can be seen, the z axis varies between 0 and 55 nm and, in these cases, Sa is necessarily different from zero. The height parameters (Table **1**), crucial for capturing the evolution of the topographic height profile configuration, demonstrate statistically similar topographic arrangements across the thin films ($p > 0.05$). The average roughness (Sa), reflecting surface deviations from the centerline, exhibits no significant variance despite a slight increase in average values from S600 to S700. This similarity in roughness distribution may stem from the films' uniform deposition process and limited grain coalescence within the evaluated temperature range. This consistent trend extends to other parameters including maximum peak height (Sp), maximum pit height (Sv), and maximum height (Sz), where no significant distinctions were observed ($p > 0.05$), reaffirming akin height distributions in the topographic profiles. It's noteworthy that although statistical differences are absent, these three parameters exhibit an incremental tendency in average values from S600 to S700, implying a potential for subtle surface differentiations on specific topographical spatial scales. This observation can be attributed to the uniform deposition process employed for the films, which indicates the absence of

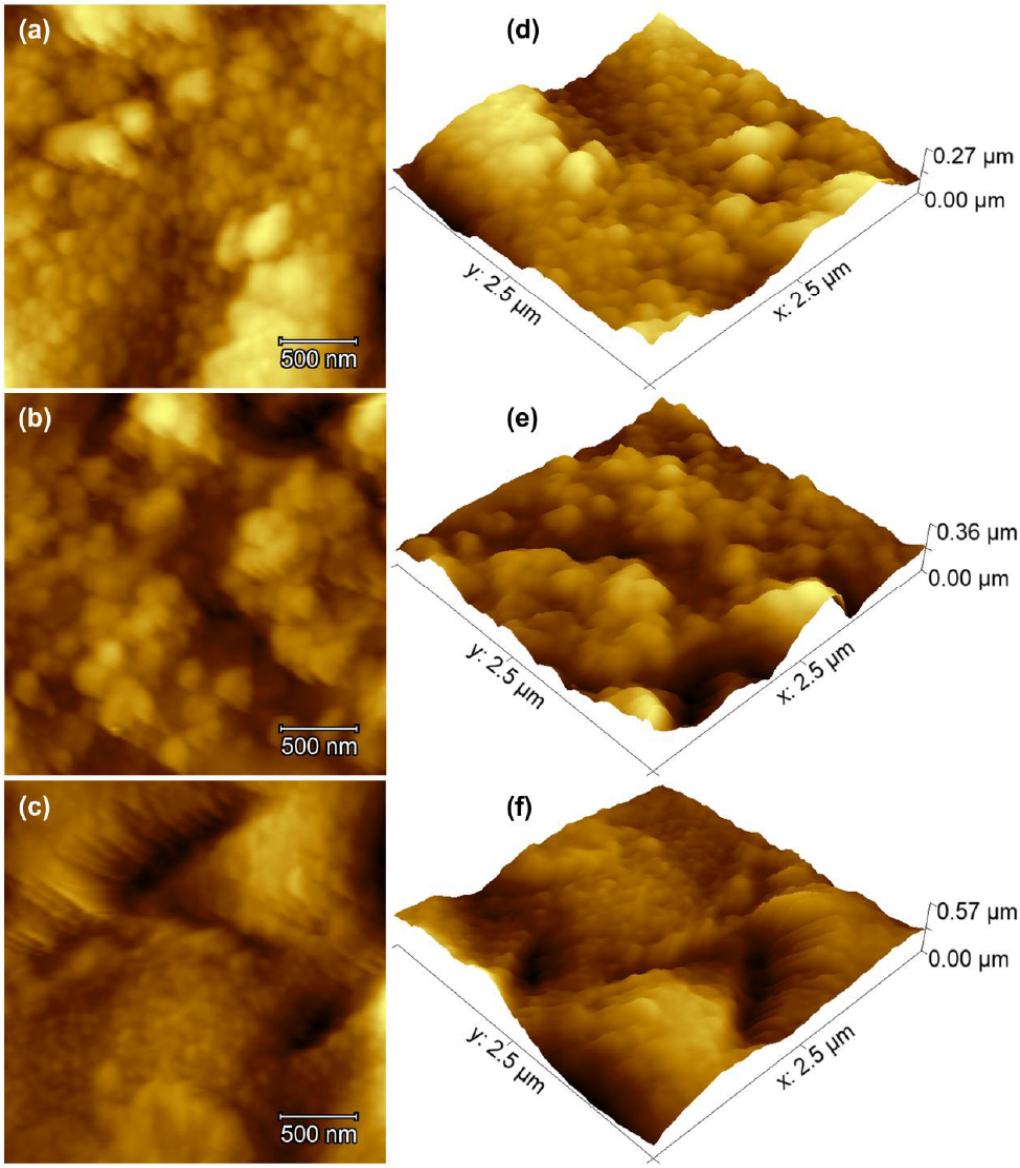

Figure 1: Relevant 2D and3D AFM micrographs of samples: **a**,**d**) S600, **b**,**e**) S650, and **c**,**f**) S700, obtained by Gwyddion, respectively.

Table 1: Height Parameters of the BNT-BT Thin Films Surface

Parameter	Unit	S600	S650	S700
Sa*	[nm]	52.3±3.7	68.1±51.9	67.9±26.8
Sp*	[nm]	216.9±28.4	235.9±99.5	308.4±81.1
Sv*	[nm]	201.7±29.8	232.1±141.2	299.7±70.9
Sz*	[nm]	418.6±46.9	468.1±227.5	608.2±145.9
S10z*	[nm]	324.1±13.3	352.8±189.6	440.2±116.7

*Samples without significant difference ANOVA One-Way and Tukey Test (p>0.05).

discontinuity points that might otherwise lead to material failure [32].

The final set of parameters is depicted using the ten-point height, a metric defined as the average height of the five highest local peaks and the average height

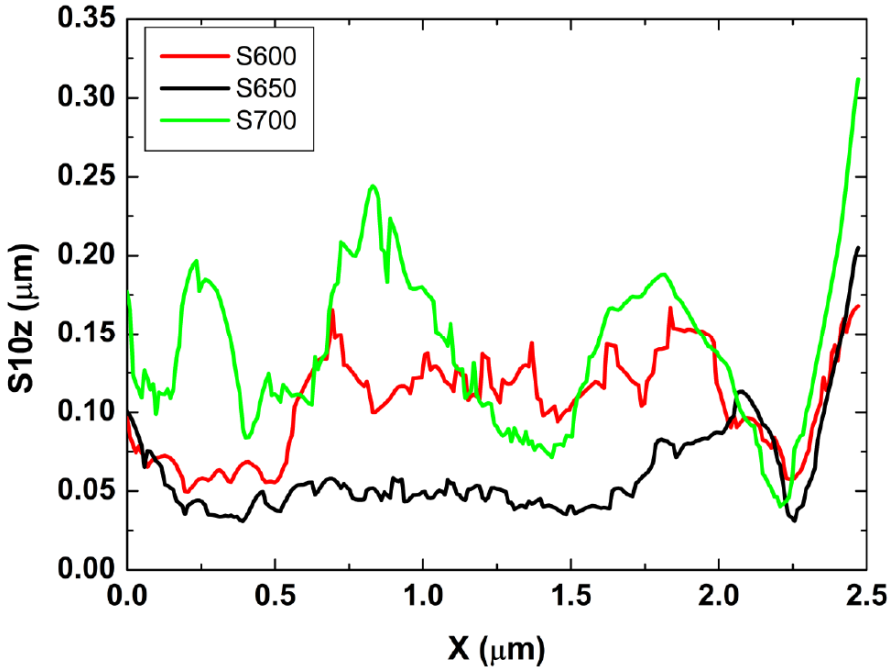

Figure 2: Ten-point height profiles obtained by Gwyddion from AFM images.

of the five lowest local valleys within the topographic profile. In essence, it quantifies the difference between the five tallest peaks and the five deepest valleys, thereby optimizing the average peak height. This indicates the presence of elevated peaks and deep troughs contributing to heightened surface roughness. The expected outcome is reflected in the Sz values, as detailed in Table **1**. Notably, the S600 sample exhibits the minimum average S10z value, at approximately 324 nm, implying a relatively smoother surface. Subsequently, S10z values increase for the S650 and S700 samples (Table **1**). The latter attains a peak average value of around 440 nm, although ANOVA analysis reveals no significant variance for this parameter either. Figure **2** portrays a representative graph of ten-point height profiles concerning their surroundings, correlated with AFM images from Figure **1**.

However, the descriptive form parameters mentioned earlier lack the ability to capture specific morphological characteristics, as they fail to differentiate between arbitrary permutations of topographic positions with varying heights. To address this, the utilization of Minkowski functionals (MFs) becomes essential in quantifying the morphometry of nanostructured surfaces [24, 33]. Minkowski functionals are instrumental in discerning spatial attributes within random fields and are adept at distinguishing diverse nanostructural models of 3D surfaces. MFs enable the exploration of morphology variations in thin film surfaces, characterized by deterministic yet stochastic behavior. MFs have been computed on the software Gwyddion 2.56 [26, 34] and they can be expressed as:

$$V = \frac{N_{white}}{N} \quad (3)$$

$$S = \frac{N_{bound}}{N} \quad (4)$$

$$X = \frac{C_{white} - C_{black}}{N} \quad (5)$$

Here, V, S, and χ correspond to Minkowski Volume, Boundary, and Connectivity, respectively. The variables on equations 3-5 represent the following: N_{white} is the count of 'white' pixels (those above the threshold), N is the total number of pixels, N_{bound} is the count of pixel boundaries between white and black regions, C_{white} is the number of continuous sets of white pixels and C_{black} is the number of continuous sets of black pixels. For thin film surfaces, these parameters probe the covered area, boundary length, and dissimilarity between connected components and voids, respectively. Figure **3** visually demonstrates the variation in Minkowski Volume, Boundary, and Connectivity for the examined surfaces as a function of normalized threshold (z). As evident, the three

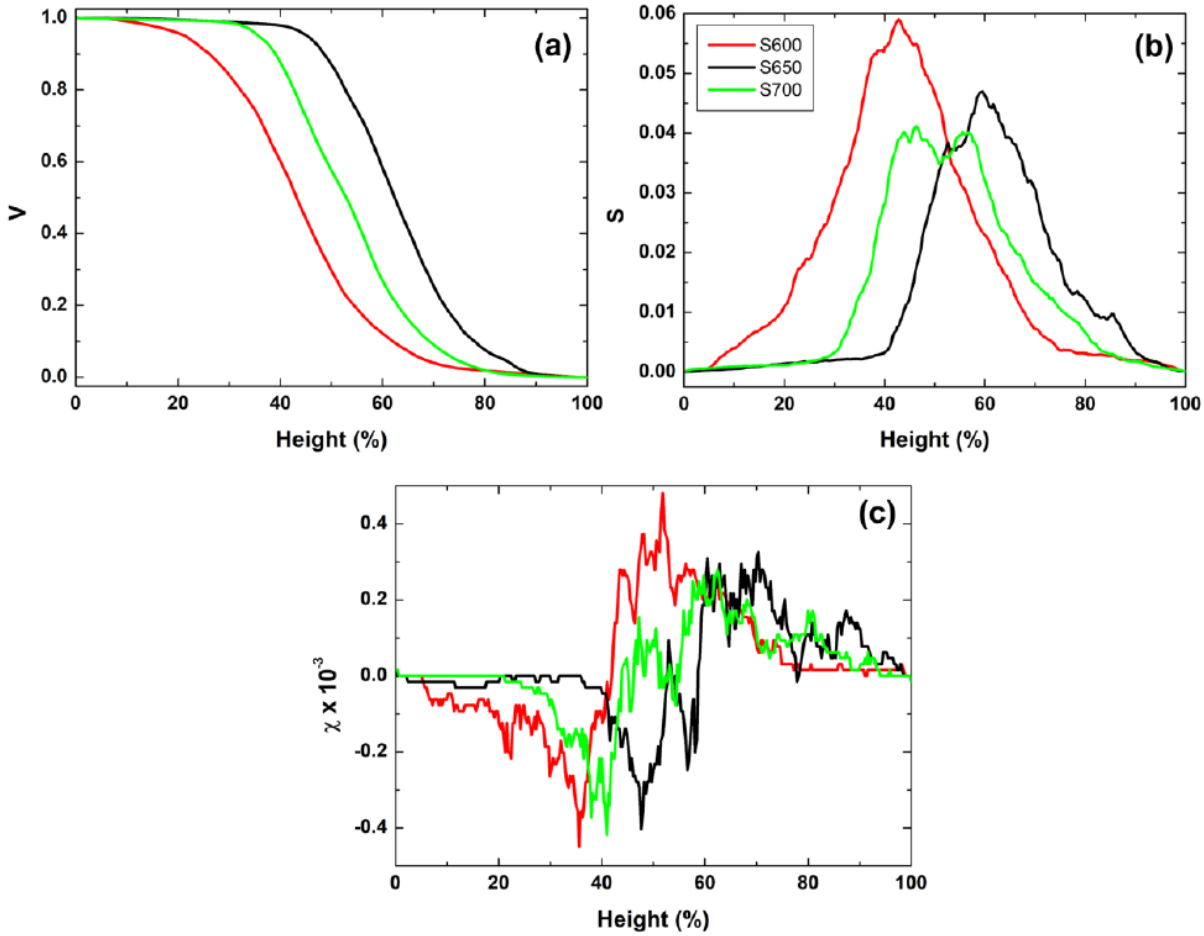

Figure 3: The MFs functionals of the samples obtained by Gwyddion: (**a**) Minkowski volume, (**b**) Minkowski boundary, and (**c**) Minkowski connectivity for S600, S650, and S700.

descriptors exhibit distinct graphical trends, underscoring the diverse morphology of the surface texture associated with various types of nanopatterned templates. This calculation relies on the separation of AFM images into two components: the high parts, which represent plateaus, and the low parts, which represent valleys [35].

The MFs, which are geometric mathematical tools widely employed for analyzing irregular morphologies [36], are depicted as curves in Figure **3a**-**c**. It's evident that these curves exhibit typical patterns characteristic of randomly rough surfaces [37]. In Figure **3**(**a**), at threshold z=0, the entire surface is encompassed, resulting in the maximum normalized Minkowski volume (V=1). As the threshold rises, fewer portions of the surface are encompassed, leading to a decrease in V. As can be seen, from S600 to S700 the curves have similar behaviors, but with decays at different height values as a function of increasing temperature, indicating that their upper and lower regions are different. Notably, the rate of decrease in V for the S600 sample surpasses that of the S650 and S700 samples. For S700, the curve begins to decrease for higher height values, showing that its surface is dominated by higher regions compared to the other 2 samples. In other words, S600 has more valleys than peaks, S650 is in an intermediate situation and S700 is dominated by peaks, which is related to the presence of larger grains on its surface, which may be a direct effect of the increase in sintering temperature. Figures **3b** and **3c** depict the Minkowski boundary and connectivity curves for the three samples, respectively, as functions of the threshold level (z). When comparing the curves in Figure **3b**, it becomes apparent that S600 exhibits a wider distribution of boundaries, suggesting a potential greater variation in surface heights, which aligns with observations in the AFM images. In contrast, the curves for S600 and S650 display less symmetrical behavior compared to S700. They exhibit narrower boundary distributions, indicating smoother surfaces with fewer height variations. The S(z) curves

approach zero as z approaches both 0% and 100%, indicating rapid growth, followed by a decline to a local minimum, and then a subsequent rapid increase leading to a maximum. This analysis underscores the intricate morphological changes that the films undergo as annealing temperatures increase.

The other functional parameter under evaluation, Minkowski connectivity, as illustrated in Figure **3c**, serves to characterize the topological structure of surface patterns by quantifying differences in the number of white and black regions within images [38]. This parameter utilizes the radially Gaussian mean power spectral density function to shed light on pattern connectivity, especially when it comes to detecting topological changes in the pattern (such as its fractal nature). For the S600 sample, the connectivity is slightly lower, but as the heat treatment temperature increases for the S650 and S700 samples, it rises. The χ connectivity value can be either positive, indicating surfaces with a higher density of peaks, or negative, suggesting a prevalence of lower regions or valleys. These variations in peak and valley values can have relevance in various technical applications. Importantly, these findings align with observations made in AFM micrographs [39].

CONCLUSIONS

This study focuses on the investigation of $Bi_{0.5}Na_{0.5}Ba(TiO_3)$ thin film morphology, synthesized via a sol-gel technique and deposited on $Pt(111)/TiO_2/SiO_2/Si$ substrates, followed by heat treatment at 600°C, 650°C, and 700°C. Morphological examination unveils distinct surface characteristics resulting from varied annealing temperatures. Interestingly, despite these morphological differences, the height parameters fail to exhibit significant variations, indicating that spatial patterns remain largely unaltered with increasing temperature. Similarly, the ten-point profile parameter also fails to display noteworthy differences among surfaces. In contrast, the utilization of Minkowski functionals in topological analysis confirms substantial morphological disparities between the samples. This underscores the capacity of morphological analysis to unravel material performance intricacies, employing microstructural shape and quantitative roughness assessment of respective surfaces. Such analytical insights hold the promise of predictive evaluations of functional behavior, including potential applications in industrial quality control during the sample manufacturing processes.

ACKNOWLEDGMENTS

The authors thank Coordenação de Aperfeiçoamento de Pessoal de Nível Superior (CAPES) and FAPEAM (Fundação de Amparo à Pesquisa do Estado do Amazonas, EDITAL N. 010/2021- CT&I ÁREAS PRIORITÁRIAS and N. 013/2022-PRODUTIVIDADE EM CT&I) for the financial support, as well as the use of the infrastructure of the Analytical Center of Universidade Federal do Amazonas (UFAM) and the infrastructure of Centro Multiusuário para Análise de Fenômenos Biomédicos of Universidade do Estado do Amazonas (CMABio - UEA). H.D.d.F.F. acknowledges funding support from CNPq Processo 306210/2022-3.

REFERENCES

[1] A.K. Tagantsev, G. Gerra, J. Appl. Phys. 100 (2006). https://doi.org/10.1063/1.2337009

[2] Metal Oxide-Based Thin Film Structures, 2018.

[3] H.Y. Lee, M.M. Al Ezzi, N. Raghuvanshi, J.Y. Chung, K. Watanabe, T. Taniguchi, S. Garaj, S. Adam, S. Gradečak, Nano Lett. 21 (2021). https://doi.org/10.1021/acs.nanolett.0c04924

[4] S.A. Dargham, F. Ponchel, N. Abboud, M. Soueidan, A. Ferri, R. Desfeux, J. Assaad, D. Remiens, D. Zaouk, J. Eur. Ceram. Soc. 38 (2018). https://doi.org/10.1016/j.jeurceramsoc.2017.06.019

[5] S.A. Dargham, F. Ponchel, Y. Zaatar, J. Assaad, D. Remiens, D. Zaouk, Mater. Today Proc. 3 (2016) 810-815. https://doi.org/10.1016/j.matpr.2016.02.013

[6] C. Sameera Devi, M. Buchi Suresh, G. Kumar, G. Prasad, Mater. Sci. Eng. B 228 (2018) 38-44. https://doi.org/10.1016/j.mseb.2017.11.005

[7] A. Prado-Espinosa, J. Camargo, A. del Campo, F. Rubio-Marcos, M. Castro, L. Ramajo, J. Alloys Compd. 739 (2018). https://doi.org/10.1016/j.jallcom.2017.12.308

[8] L. Wu, S. Zhang, J. Liu, Q. Hu, J. Chen, Y. Wang, B. Xu, Y. Xia, J. Yin, Z. Liu, Ceram. Int. 42 (2016).

[9] P. Li, B. Liu, B. Shen, J. Zhai, L. Li, H. Zeng, Ceram. Int. 43 (2017) 1008-1013. https://doi.org/10.1016/j.ceramint.2016.10.033

[10] F.M. Mwema, O.P. Oladijo, T.S. Sathiaraj, E.T. Akinlabi, Mater. Res. Express 5 (2018). https://doi.org/10.1088/2053-1591/aabe1b

[11] J. Song, Y. Zhou, N.P. Padture, B.D. Huey, Nat. Commun. 11 (2020). https://doi.org/10.1038/s41467-020-17685-5

[12] A. Grayeli Korpi, Ş. Ţălu, M. Bramowicz, A. Arman, S. Kulesza, B. Pszczolkowski, S. Jurečka, M. Mardani, C. Luna, P. Balashabadi, S. Rezaee, S. Gopikishan, Mater. Res. Express 6 (2019) 086463. https://doi.org/10.1088/2053-1591/ab26be

[13] Y.L. Lighvan, Vak. Forsch. Und Prax. 34 (2022) 38-43. https://doi.org/10.1002/vipr.202200781

[14] Ş. Ţălu, R.S. Matos, E.P. Pinto, S. Rezaee, M. Mardani, Surfaces and Interfaces 21 (2020) 100650. https://doi.org/10.1016/j.surfin.2020.100650

[15] H. Aminirastabi, H. Xue, V. V. Mitić, G. Lazović, G. Ji, D. Peng, Mater. Chem. Phys. 239 (2020) 122261. https://doi.org/10.1016/j.matchemphys.2019.122261

[16] K. Ghosh, R.K. Pandey, Appl. Phys. A Mater. Sci. Process. 125 (2019). https://doi.org/10.1007/s00339-019-2398-y

[17] R. Shakoury, S. Rezaee, F. Mwema, C. Luna, K. Ghosh, S. Jurečka, Ş. Ţălu, A. Arman, A. Grayeli Korpi, Opt. Quantum Electron. 52 (2020). https://doi.org/10.1007/s11082-020-02388-4

[18] C. Yago Pereira Batista, Y. Romaguera-Barcelay, R.S. Matos, A. dos Santos Atherly Pedraça, M. do Amaral Amâncio, A. Kourouma, Y. Leyet Ruiz, E. Adriano Cotta, W. Ricardo Brito, A. María Dip Gandarilla, M. Valério Botelho do Nascimento, F. Xavier Nobre, N. Santos Ferreira, M. Salerno, H. Duarte da Fonseca Filho, Appl. Surf. Sci. 615 (2023). https://doi.org/10.1016/j.apsusc.2023.156374

[19] S. Carlos, L. De, O. Melo, P. Dra, J. Agnieszka, M. Pawlicka, (2010).

[20] D. Nečas, P. Klapetek, Cent. Eur. J. Phys. 10 (2012) 181-188. https://doi.org/10.2478/s11534-011-0096-2

[21] Ş. Ţălu, S. Stach, S. Valedbagi, R. Bavadi, S.M. Elahi, M. Ţălu, Mater. Sci. 33 (2015) 541-548. https://doi.org/10.1515/msp-2015-0086

[22] R.S. Matos, B.S. Pinheiro, I.S. Souza, R.R. Paes de Castro, G.Q. Ramos, E.P. Pinto, R.S. Silva, H.D. da Fonseca Filho, Micron 142 (2021). https://doi.org/10.1016/j.micron.2020.102996

[23] Y.R. Barcelay, J.A.G. Moreira, A. de Jesus Monteiro Almeida, W.R. Brito, R.S. Matos, H.D. da Fonseca Filho, Mater. Lett. 279 (2020) 128477. https://doi.org/10.1016/j.matlet.2020.128477

[24] W.S. da Conceição, Ş. Ţălu, R.S. Matos, G.Q. Ramos, F.G. Zayas, H.D. da Fonseca Filho, Microsc. Res. Tech. 84 (2021). https://doi.org/10.1002/jemt.23699

[25] F. Blateyron, Characterisation of Areal Surface Texture, Springer-Verlag Berlin Heidelberg, Berlin, Germany, 2013.

[26] Ş. Ţălu, S. Stach, T. Ghodselahi, A. Ghaderi, S. Solaymani, A. Boochani, Ż. Garczyk, J. Phys. Chem. B 119 (2015) 5662-5670. https://doi.org/10.1021/acs.jpcb.5b00042

[27] S. Stach, Ş. Ţălu, R. Dallaev, A. Arman, D. Sobola, M. Salerno, Silicon 12 (2020). https://doi.org/10.1007/s12633-019-00351-x

[28] D. Sobola, P. Kaspar, J. Oulehla, S. ťalu, N. Papež, Mater. Sci. Pol. (2020).

[29] G. Zaneta, S. Sebastian, T. Ştefan, S. Dinara, W. Zygmunt, J. Biomimetics, Biomater. Biomed. Eng. 31 (2017) 1-10.

[30] O.A. González-Meza, E.R. Larios-Durán, A. Gutiérrez-Becerra, N. Casillas, J.I. Escalante, M. Bárcena-Soto, J. Solid State Electrochem. 23 (2019). https://doi.org/10.1007/s10008-019-04410-6

[31] J. Zhao, N. Zhang, W. Ren, G. Niu, D. Walker, P.A. Thomas, L. Wang, Z.G. Ye, J. Am. Ceram. Soc. 102 (2019).

[32] R.S. Matos, G.A.C. Lopes, N.S. Ferreira, E.P. Pinto, J.C.T. Carvalho, S.S. Figueiredo, A.F. Oliveira, R.R.M. Zamora, Arab. J. Sci. Eng. 43 (2018). https://doi.org/10.1007/s13369-017-3024-y

[33] Ş. Ţălu, Polym. Eng. Sci. (2013) n/a-n/a.

[34] D. Nečas, P. Klapetek, Cent. Eur. J. Phys. 10 (2012) 181-188. https://doi.org/10.2478/s11534-011-0096-2

[35] M. Salerno, M. Banzato, Microsc. Anal. 19 (2005) 13-15.

[36] C.H. Arns, M.A. Knackstedt, K.R. Mecke, Colloids Surfaces A Physicochem. Eng. Asp. 241 (2004) 351-372. https://doi.org/10.1016/j.colsurfa.2004.04.034

[37] J. Schmähling, F.A. Hamprecht, Wear 262 (2007). https://doi.org/10.1016/j.wear.2007.01.025

[38] F.M. Mwema, E.T. Akinlabi, O.P. Oladijo, Lect. Notes Mech. Eng. (2020) 251-263. https://doi.org/10.1007/978-981-13-8297-0_28

[39] Ş. Ţălu, P. Nikola, D. Sobola, A. Achour, S. Solaymani, J. Mater. Sci. Mater. Electron. 28 (2017). https://doi.org/10.1007/s10854-017-7422-4

Received on 13-08-2023 Accepted on 20-09-2023 Published on 21-09-2023

DOI: https://doi.org/10.31875/2410-4701.2023.10.09